Atmospheric and Oceanic Science Letters 15 (2022) 100194

KeAi
CHINESE ROOTS
GLOBAL IMPACT

Contents lists available at ScienceDirect

Atmospheric and Oceanic Science Letters

journal homepage:
http://www.keaipublishing.com/en/journals/atmospheric-and-oceanic-science-letters/

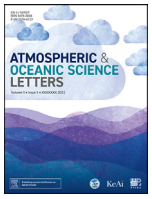


# Evaluation of the Madden–Julian oscillation in HiRAM


Jie Jiang[a], Lu Wang[a,b,*], Jiuwei Zhao[a], Tim Li[c,a]

[a] Key Laboratory of Meteorological Disaster, Ministry of Education (KLME)/Joint International Research Laboratory of Climate and Environmental Change (ILCEC)/Collaborative Innovation Center on Forecast and Evaluation of Meteorological Disasters (CIC-FEMD), Nanjing University of Information Science and Technology, Nanjing, China
[b] Laboratory for Regional Oceanography and Numerical Modeling, Qingdao National Laboratory for Marine Science and Technology, Qingdao, China
[c] International Pacific Research Center, University of Hawai'i at Mānoa, Honolulu, USA

ARTICLE INFO

*Keywords:*
Madden–Julian oscillation
Moist static energy
Eastward propagation
HiRAM
关键词:
季节内振荡
湿静力能
东传
HiRAM

ABSTRACT

The aim of this study was to understand the cause of Madden–Julian oscillation (MJO) bias in the High Resolution Atmospheric Model (HiRAM) driven by observed SST through process-oriented diagnosis. Wavenumber-frequency power spectrum and composite analyses indicate that HiRAM underestimates the spectral amplitude over the MJO band and mainly produces non-propagating rather than eastward-propagating intraseasonal rainfall anomalies, as observed. Column-integrated moist static energy (MSE) budget analysis is conducted to understand the MJO propagation bias in the simulation. It is found that the bias is due to the lack of a zonally asymmetric distribution of the MSE tendency anomaly in respect to the MJO convective center, which is mainly attributable to the bias in vertical MSE advection and surface turbulent flux. Further analysis suggests that it is the unrealistic simulation of MJO vertical circulation anomalies in the upper troposphere as well as overestimation of the Rossby wave response that results in the bias.

摘要

本研究评估了高分辨率大气环流模式HiRAM模拟的MJO. 结果表明, HiRAM模拟的MJO东传很弱. 我们通过计算整层积分的湿静力能 (MSE) 收支来诊断MJO东传模拟偏差的原因. 结果发现, MSE倾向相对于MJO对流中心的纬向非对称分布很弱是导致东传模拟偏弱的原因, 这主要是由MSE垂直平流和地表湍流通量的模拟偏差造成的. 进一步研究表明, 对流层上层MJO垂直环流结构的模拟偏差和MJO对流西侧的Rossby波环流偏强共同导致了模式的偏差. 本研究中指出的MJO传播模拟偏差的原因与之前基于多模式结果的结论不同, 这意味着要想了解特定模式的模拟偏差, 有必要对该模式进行具体分析.

## 1. Introduction

The Madden–Julian oscillation (MJO) is characterized by planetary-scale circulation coupled with convection propagating eastward along the equator. It is the most dominant intraseasonal variability in the tropics, showing a broad spectral peak over a 20–70-day time scale (see reviews by Zhang (2005) and Li (2014)). The MJO convection is usually initiated and enhanced in the Indian Ocean, weakens over the Maritime Continent, re-intensifies over the western Pacific, and dies out upon reaching the central Pacific. The convection is associated with a Kelvin–Rossby wave couplet (Li and Wang, 1994; Wang and Chen, 2017) or a quadrupole structure (Zhang and Ling, 2012) in horizontal circulations, as well as a baroclinic vertical structure tilted with altitude.

The activity of the MJO in different phases can exert significant influence on global weather and climate through circulation anomalies (e.g., Li et al., 2020). For example, the MJO may trigger the onset of the Asian monsoon as it moves across the Indian Ocean and Maritime Continent (e.g., Zhou and Chan, 2005). Wind perturbations associated with the MJO could trigger the onset of El Niño events (e.g., Kessler and Kleeman, 2000). Tropical cyclones occur more frequently during the active MJO phase than the suppressed phase (Sobel and Maloney, 2000; Zhao and Li, 2019). Thus, the MJO is regarded as an important source of predictability for extended-range weather and climate forecasting, which remains a big challenge for currently for operational and research communities (Xiang et al., 2015; Zhu and Li, 2017).

Unfortunately, the ability of current general circulation models (GCMs) to simulate the MJO is limited and the bias has been pervasive over recent generations of climate models participating in the Coupled Model Intercomparison Project (Ahn et al., 2020), since most of them cannot successfully capture even the basic propagation features of the MJO. For instance, Jiang et al. (2015) reported that three quarters of the 27 models in their analysis show a dominant intraseasonal mode over

* Corresponding author.
*E-mail address:* luwang@nuist.edu.cn (L. Wang).

https://doi.org/10.1016/j.aosl.2022.100194
Received 20 December 2021; Revised 2 February 2022; Accepted 3 February 2022
Available online 17 February 2022

the tropical Indo-Pacific regions with stationary or westward propagation, while only a few show a dominant mode with eastward propagation, as observed.

Numerous studies have attempted to identify the key biases in models that prevent them from reproducing the eastward propagation of the MJO. One important factor is the cumulus parameterization scheme, including the triggering function, mixing assumption, rain re-evaporation, closure assumption, and convective momentum transport (see review by Kim and Maloney (2017)). Another factor is the poor simulation of the three-dimensional structure of the MJO circulation. Observationally, the vertical velocity anomalies exhibit a second-baroclinic mode vertical structure east (west) of the MJO convection, with descending (ascending) anomalies in the upper troposphere and ascending (descending) anomalies in the boundary layer, while the lower-tropospheric horizontal circulations show poleward (equatorward) meridional wind anomalies. As the mean moist static energy (MSE) profile shows a minimum in the middle troposphere and maximum near the equator and the mean moisture maximizes near the equator over the warm pool region, such circulation anomalies could induce positive (negative) MSE tendency anomalies to the east (west) of the MJO convection, which is favorable for the eastward propagation of the MJO (e.g., Wang et al., 2017).

Recently, more and more studies have begun to emphasize the importance of simulating the lower-tropospheric mean moisture over the Indian Ocean and western Pacific Ocean in producing reasonable MJO propagation, as the horizontal MSE advection is primarily related to the MJO wind anomalies acting on the mean moisture gradient (e.g., Gonzalez and Jiang, 2017; Chen et al., 2022). A significant linear relationship is found between the simulation skill of the mean moisture and that of the MJO eastward propagation.

It is worth mentioning that these results were based on multi-model evaluations, by comparing the composite difference between the best and the poorest model groups. Although such a strategy is helpful toward understanding the general features of many models, whether it is applicable in understanding the bias of a single model is unknown. An interesting question arises if a model can capture the observed climatology of the moisture very well, insofar as could it also simulate the MJO propagation reasonably? If not, what is the key bias responsible for the poor simulation?

To address these questions, this study evaluated a simulation based on an atmospheric general circulation model (AGCM) from the Geophysical Fluid Dynamics Laboratory, named HiRAM-C180, which has been shown to be good at capturing the climatological intensity and distribution of precipitation (Fig. S1), as well as the seasonal and interannual variabilities of tropical cyclones over the globe (Zhao et al., 2009; Murakami et al., 2015). In this paper, after describing in Section 2 the data and methods employed in the study, we first evaluate the simulation of the MJO by HiRAM (Section 3), and then report results from carrying out a process-oriented diagnosis of the simulation to identify the specific reason for the model bias (Section 4). In this way, we are able to set a clear goal for future improvement of this model.

## 2. Data and methods

HiRAM-C180 is a high-resolution AGCM with 32 vertical levels and a horizontal resolution of roughly 50 km (varying between 43.5 and 61.6 km). The model physics and other details can be referred to in Zhao et al. (2009) and the model code can be obtained from https://www.gfdl.noaa.gov/hiram-quickstart/. An experiment was conducted using the observed monthly SST from 1980 to 2009 as the oceanic boundary condition and the model was integrated for 30 years with daily outputs of atmospheric variables for diagnosing the MJO. The dataset used in this paper was interpolated onto a $2^\circ \times 2^\circ$ grid through bilinear interpolation for further analysis. As the MJO is a planetary-scale phenomenon, the results in the current study are not sensitive to a change in data resolution.

The verification data include: (1) daily rainfall observations provided by GPCP with a horizontal resolution of $1^\circ \times 1^\circ$ (Huffman et al., 2001); (2) daily OLR observations provided by NOAA (Liebmann and Smith, 1996); and (3) daily zonal wind, temperature, sensible heat flux, and other physical quantities provided by ERA-Interim (Dee et al., 2011). The time span for these datasets is 1997–2008 and the datasets from NOAA and ERA-Interim are interpolated to horizontal grids at $2.5^\circ \times 2.5^\circ$.

Previous studies have demonstrated that diagnosis of the intraseasonal column-integrated MSE equation could reveal the key processes involved in the MJO's eastward propagation (e.g., Wang et al., 2017). Therefore, in this study we calculated the MSE budget of both the simulated and observed results, and then identified their main differences. According to the intraseasonal column-integrated MSE budget equation (see details in the supplementary material), the MSE tendency is contributed by vertical and horizontal advections, surface latent and sensible heat fluxes, and shortwave and longwave radiative heating rates.

## 3. MJO simulation in HiRAM

Fig. 1 shows the wavenumber-frequency power spectra of 10°S–10°N averaged precipitation and 850-hPa zonal wind ($U$850) during boreal winter (November–April). The observed spectral power of precipitation and $U$850 show a maximum over the domain of eastward wavenumbers 1–3 and a period of 20–70 days. The simulated spectral power of precipitation and $U$850 within the MJO band is much smaller than in the observation, and the maximum spectral power is seen in the lower-frequency band (period larger than 70 days). The eastward/westward power spectrum ratio (E/W ratio) is further calculated by dividing the sum of the spectral power over the domain of eastward wavenumbers 1–3 and period of 20–70 days by that of its westward propagating counterpart. The observed (simulated) E/W ratio is ~2.2 and ~3.0 (1.6 and 1.7) for precipitation and $U$850. The results suggest that HiRAM simulates weaker eastward propagation of convection and circulation than observed. Because the peak of the observed power spectrum is confined within the period of 20–70 days, we use a 20–70 day bandpass filter (Duchon, 1979) to extract the intraseasonal component in this study. This is in contrast to some studies that have used a 20–100 day filter (e.g., Jiang et al., 2015; Kim et al., 2014; Wang et al., 2017), as we believe it is better to exclude the signals from the lower frequency. Prior to filtering, the first four harmonics of the daily annual cycle were removed.

Then, multivariate EOF analysis of the 20–70 day filtered OLR, $U$850, and $U$200 anomalies averaged over 15°S–15°N was performed for the observation and simulation, separately (see Fig. S2). In the observation, the first two modes, with one convection center near 120°E and the other near 80°E, show a coupled structure of convection and circulation (convergence at the lower level and divergence at the upper level), and they account for nearly equal fractional variance (23.6% and 22.3%). In the simulation, the two modes account for smaller fractional variances, with one being 15.0% and the other 11.6%. The convection amplitude near the western Pacific is simulated well, while that near the Indian Ocean is much lower. The time series of principle components corresponding to the first two EOF modes are used to define eight MJO phases following Wheeler and Hendon (2004). Fig. 2 displays the composite 20–70 day filtered rainfall anomalies and 850 hPa wind field in eight phases. In the observation, the MJO convection starts over the Indian Ocean in phases 1–3, passes through the Maritime Continent in phases 4–5, and into the western Pacific in phases 6–7, before disappearing near the date line in phase 8. In the simulation, however, the magnitude of MJO convection is much weaker. In phases 6–8, the convection seems less mobile.

Fig. 3 shows lag-longitude diagrams of 10°S-10°N averaged rainfall and column-integrated MSE regressed onto an intraseasonal rainfall index for the observation and the simulation, separately. The rainfall index was calculated by the intraseasonal rainfall anomalies averaged over the equatorial Indian Ocean (5°S–5°N, 75°–85°E). Raw fields were regressed

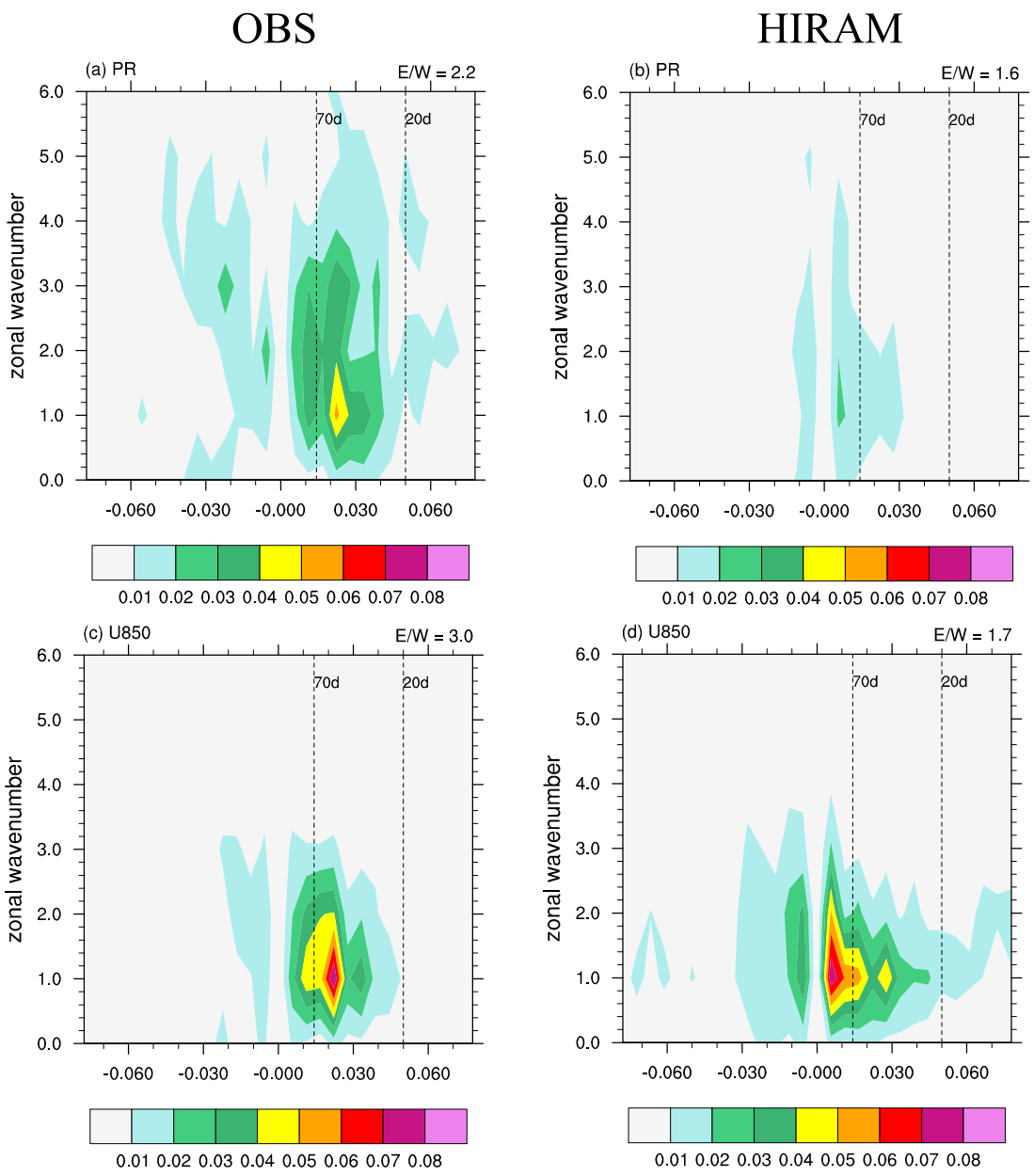


**Fig. 1.** (a) Wavenumber-frequency power spectra of precipitation averaged over 10°S–10°N based on GPCP. (b) As in (a) except for *U*850 based on ERA-interim. (c, d) As in (a, b) but based on the HiRAM simulation. The E/W ratio calculated for each variable is labeled in the upper-right corner of the corresponding panel.

onto the index, and the regressed coefficients were multiplied by 3 so that the regressed fields represent the response to 3 mm $d^{-1}$ rainfall anomalies. For the observation, the rainfall anomalies exhibit continuous eastward propagation (Fig. 3(a)), while the simulated precipitation seems stationary over the Indian Ocean (Fig. 3(b)). The evolution of column-integrated MSE anomalies follows that of the rainfall anomalies very well.

To sum up, HiRAM simulates much weaker MJO signals than observed, and little eastward propagation.

## 4. MSE budget analysis

To understand the cause of the biased propagation, an MSE budget analysis was conducted. The details of this method can be found in the supplementary material Fig. 4. shows the horizontal patterns of column-integrated MSE tendency anomalies overlaid by the MSE anomaly at lag zero for the observation and the simulation, separately. The observation (Fig. 4(a)) shows a zonally asymmetric MSE tendency with a positive (negative) tendency anomaly to the east (west) of the maximum MSE anomaly (near 80°E). Such an asymmetric structure of the MSE tendency anomaly favors the eastward propagation of the positive MSE anomaly. However, a positive tendency anomaly exists on both sides of the maximum MSE anomaly and no asymmetrical structure is exhibited in the simulation (see Fig. 4(b)), which is consistent with the non-propagating characteristic found in Fig. 3(b).

As the zonal distribution of the MSE tendency anomaly relative to the convective center is critical to the propagation, we therefore compared the east–west difference in each MSE tendency term for the observation and the simulation. Each term in Eq. (S1) was calculated and regressed onto the intraseasonal rainfall index, and then the regressed fields were averaged over (10°S–10°N, 40–70°E) and (10°S–10°N, 110°–160°E), which were located to the west and east of the convective center, respectively. The selection of the two boxes followed Wang and Li (2020a). Fig. 4(c, d) show the domain-averaged results of each ten-

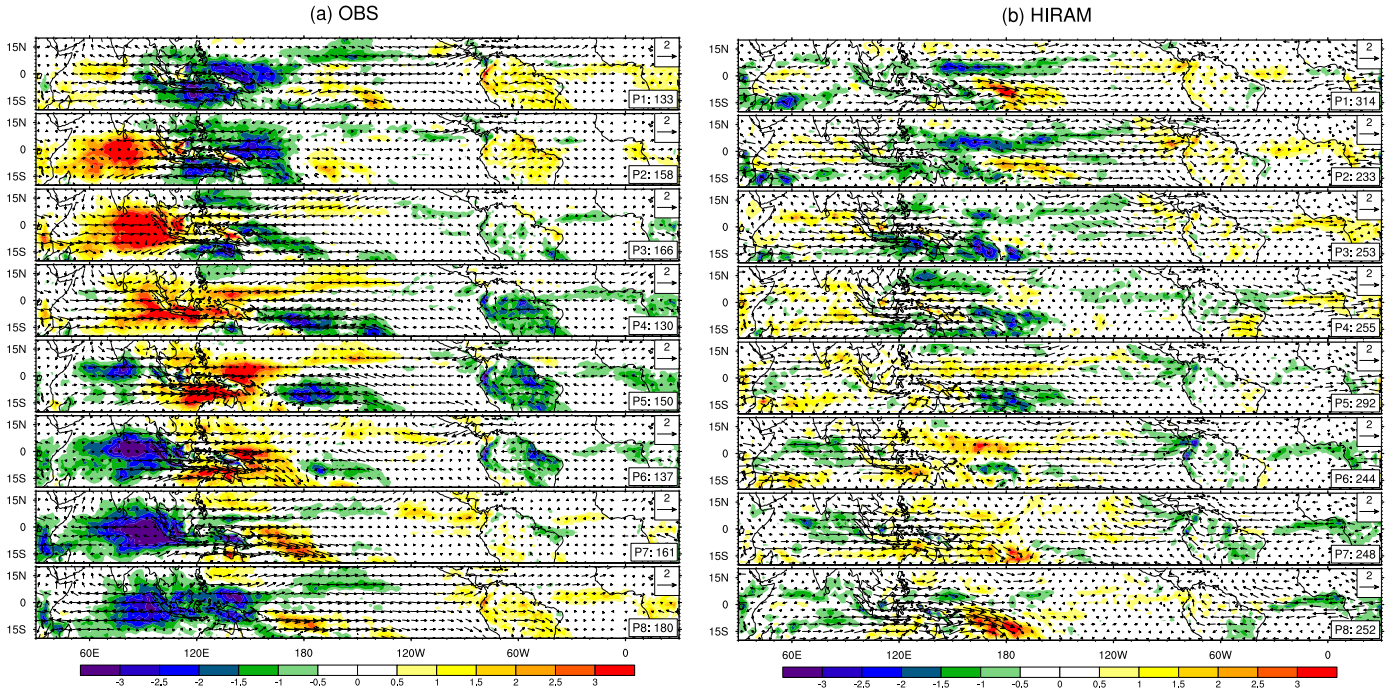


**Fig. 2.** 20–70 day filtered precipitation (shading; units: mm $d^{-1}$) and 850 hPa circulation (vectors; units: m $s^{-1}$) anomalies in eight phases. Results are based on (a) the observation and (b) the simulation.

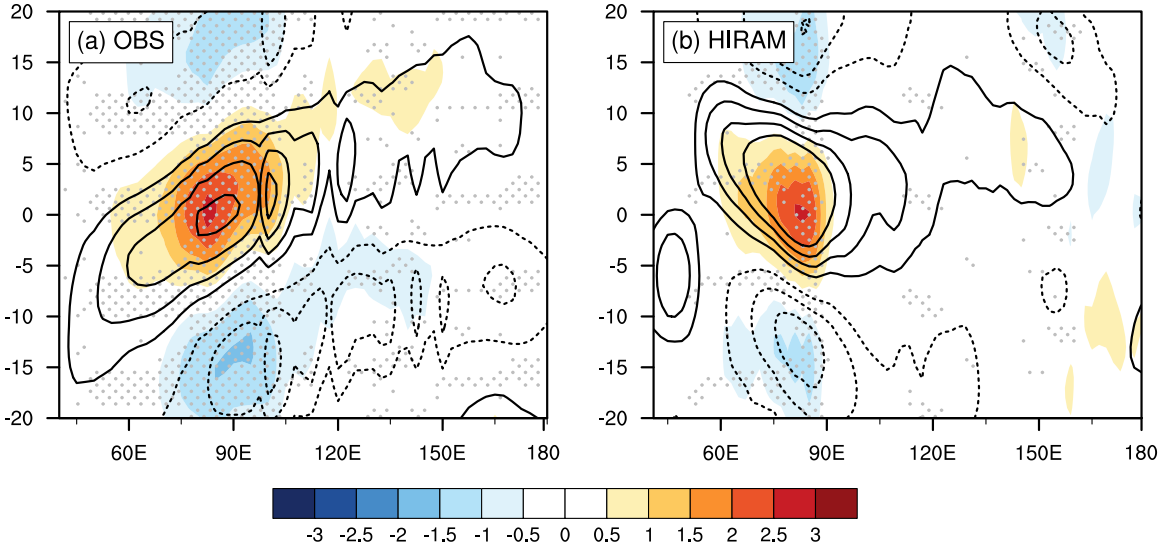


**Fig. 3.** Lag-longitude diagrams of precipitation (shading; units: 3 mm $d^{-1}$) and column-integrated MSE (contours; units: J $m^{-2}$; contour interval: $1 \times 10^6$, with the zero line omitted) averaged over 10°S–10°N regressed onto an intraseasonal rainfall index for (a) the observation and (b) the simulation. The regions exceeding the 90% confidence level are stippled.

dency term for the observation and the simulation, respectively. As shown in Fig. 4(c), the zonally asymmetric MSE tendency anomaly is mainly contributed by the vertical advection and horizontal advection terms, while the surface turbulent fluxes ($Q_t$) and column radiative heating ($Q_r$) play a negative role. However, in the simulation (Fig. 4(d)), the sign of the MSE tendency anomaly over the western box is reversed and the positive anomaly over the eastern box is much reduced compared to the observation, such that the zonal asymmetry of the MSE tendency anomaly nearly disappears. It is clear that the bias is primarily due to the vertical advection term over the western box, which is close to zero in the simulation. Beside the vertical advection, the $Q_t$ is quite different between the observation and simulation, especially west of the convection. The east–west box-averaged difference in each term is further shown in Fig. 4(e, f). As we can see, the lack of zonal asymmetry in the MSE tendency anomaly in the simulation relative to the observation is mainly contributed by the vertical advection term, while the horizontal advection term seems to be similar to the observation. In addition, $Q_t$ plays a larger negative role compared to the observation, which especially arises from the western box. Thus, we focus on the vertical advection of MSE and $Q_t$ in the following analysis to investigate the key bias of the simulation. Note that the residual term is negligible in the observation, which gives us confidence to use the budget analysis to identify the key processes for the MJO propagation. However, it is larger in the simulation, and the reason for that is not clear.

Fig. 5(a, b) display the horizontal patterns of regressed day-0 column-integrated vertical advection of MSE for the observation and

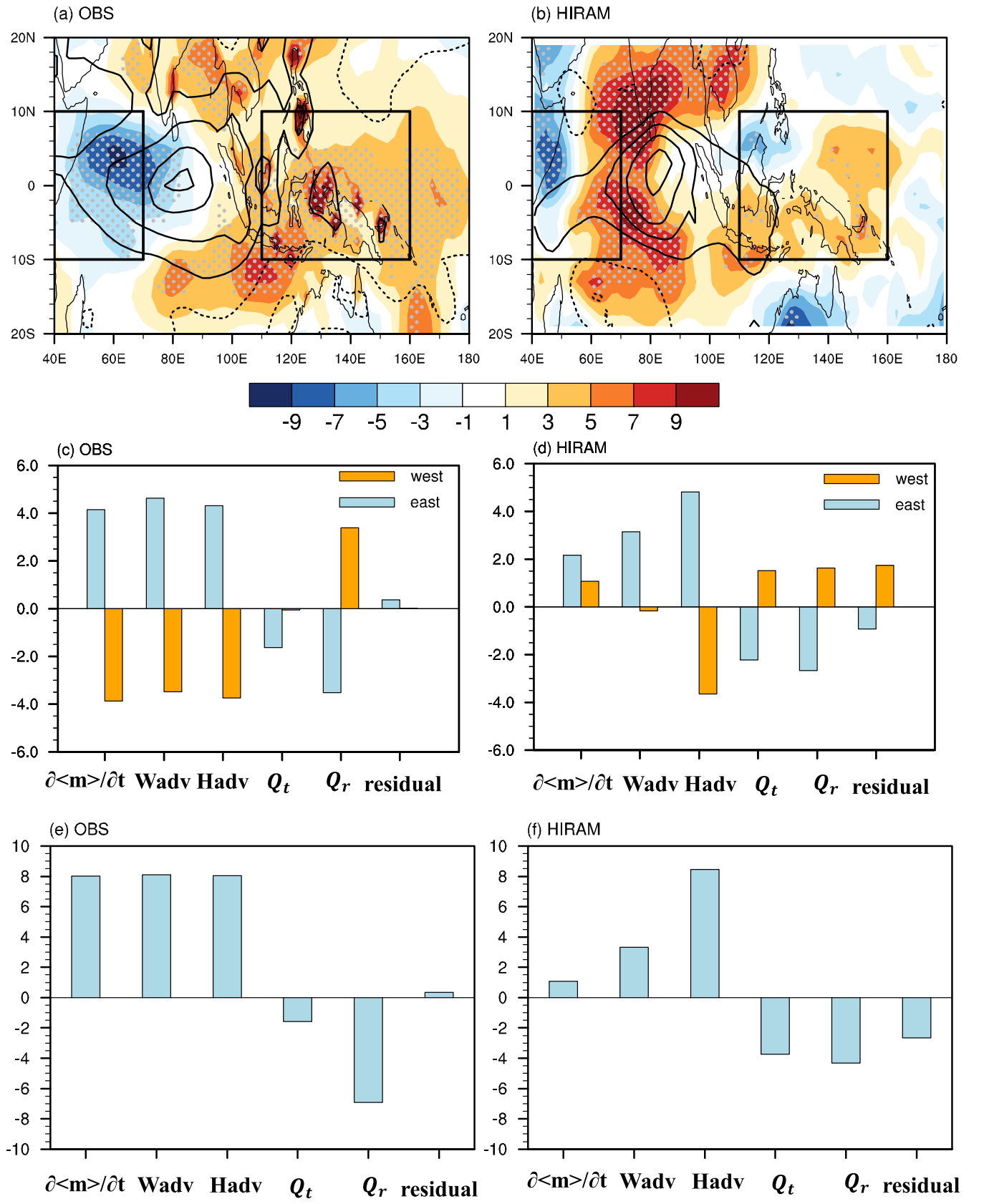


**Fig. 4.** (a, b) Horizontal pattern of MSE tendency (shading; units: W $m^{-2}$) and MSE (contours; units: J $m^{-2}$; interval: $2 \times 10^6$, with the zero line omitted) anomalies integrated in columns at lag zero. The boxes to the west and east of the MJO center indicate the regions of (10°S–10°N, 40°–70°E) and (10°S–10°N, 110°–160°E), respectively. The regions exceeding the 90% confidence level are stippled. (c, d) MSE tendency terms averaged over the eastern box (blue) and western box (orange), and (e, f) the difference between the eastern and western box average results. Bars from left to right represent MSE tendency ($\partial$<m>/$\partial$t), vertical MSE advection (Wadv), horizontal MSE advection (Hadv), surface turbulent flux ($Q_t$), column radiative heating ($Q_r$), and the residual term, respectively. The left-hand panels are calculated for the observation while the right-hand ones are for the simulation.

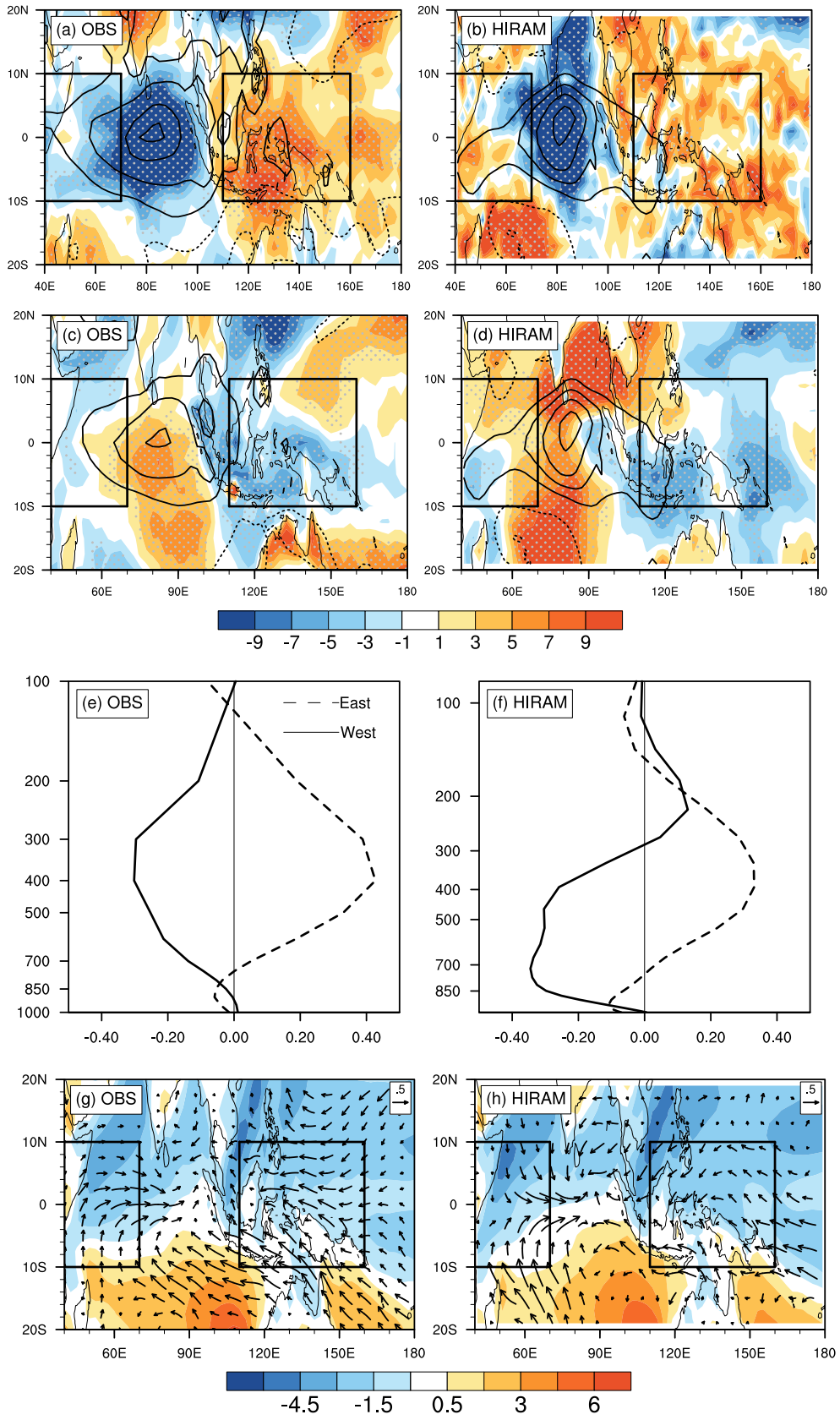


**Fig. 5.** (a, b) Horizontal pattern of vertical MSE advection (shading; units: W $m^{-2}$) and MSE (contours; units: J $m^{-2}$; interval: $2 \times 10^6$, with the zero line omitted) anomalies integrated in columns at lag zero. The boxes to the west and east of the MJO center indicate the regions of (10°S–10°N, 40°–70°E) and (10°S–10°N, 110°–160°E), respectively. (c, d) As in (a, b) except that the shading denotes $Q_1$ (units: W $m^{-2}$). (e, f) Profiles of the regressed day-0 pressure velocity anomaly averaged over the western box (solid) and the eastern box (dashed). (g, h) Horizontal distribution of the regressed 1000 hPa wind anomalies (vectors; units: m $s^{-1}$) and the climatology of meridional wind in boreal winter (shaded). The regions exceeding the 90% confidence level are stippled. The left-hand panels are calculated for the observation and the right-hand ones for the simulation.

the simulation, respectively. A zonal dipole along the equator is clearly shown in the observation, with a positive anomaly to the east of the convective center and negative anomaly at and to the west. In the simulation, however, only the negative anomaly at the convective center is clear, while the positive anomaly to the east is not organized well and no negative anomaly is seen to the west. As the vertical MSE advection is dominated by the intraseasonal vertical wind anomaly acting on the climatological MSE vertical gradient (figure not shown), we compared the vertical structures of the regressed pressure velocity anomaly in the observation and the simulation, and the results are presented in Fig. 5(e, f). In the observation (Fig. 5(c)), an apparent zonally asymmetric pattern is visible: downward (upward) anomalies in the upper troposphere appear to the east (west) of the rainfall center (80°E). The discrepancy in the vertical velocity between the observation and the simulation is primarily from the upper troposphere to the west of the rainfall center, where the simulation mainly exhibits downward anomalies. So, there is no asymmetry in the upper troposphere in HiRAM.

Fig. 5(c, d) compare the horizontal patterns of regressed $Q_t$ for the observation and the simulation, respectively. In the observation, the negative anomaly of $Q_t$ is to the east of the convection and the positive anomaly is near the convection center. Such a zonal distribution can be attributed to the superposition of the MJO-induced zonal wind anomaly and the mean zonal wind (Wang and Li, 2020b). In comparison, the positive $Q_t$ anomaly over the western box is overestimated in the simulation, especially over the northern and southern Indian Ocean. It is found that the zonal wind component plays little role in the discrepancy of the $Q_t$ anomaly (figures not shown), which is primarily due to the meridional wind component. Fig. 5(g, h) show the MJO-induced wind anomaly (vector) and mean meridional wind (shaded) at 1000 hPa for the observation and the simulation, respectively. As we can see, the observed mean meridional wind is equatorward over the Indian Ocean. Since the MJO-induced Rossby wave circulation west of the convection center also shows an equatorward wind anomaly, it would enhance the total wind speed and therefore lead to more evaporation. In the simulation, the mean meridional wind resembles the observation very well but the Rossby wave response is notably overestimated, especially over the Arabian Sea and east of Madagascar. Therefore, the wind speed over the northern and southern Indian Ocean would be overestimated in the simulation and lead to a positive $Q_t$ anomaly.

To sum up, the detailed MSE budget analysis indicates that the non-propagating characteristic of the intraseasonal rainfall anomaly in the HiRAM simulation primarily results from the unrealistic structure of the MJO vertical circulation anomaly as well as the overestimated Rossby wave circulation.

## 5. Summary and discussion

As an important source of intraseasonal prediction, the MJO remains poorly represented in most current state-of-the-art GCMs. In this study, we evaluated an AMIP-type simulation generated by HiRAM-C180 in simulating the characteristics of the MJO. This model has been demonstrated to be good at capturing the climatological tropical precipitation and the variability of tropical cyclones.

By examining the wavenumber-frequency spectral power of equatorial rainfall and *U*850, it was found that the signals over the MJO band are severely underestimated relative to the observation. The intraseasonal rainfall anomalies and 850 hPa wind anomalies in eight phases further showed that the intraseasonal rainfall anomalies in the simulation are poorly organized over the Indo-Pacific oceans and show little movement. The lagged time–longitude diagram of the intraseasonal rainfall anomaly also indicated non-propagating characteristics. By conducting an MSE budget analysis, it was found that the biased MJO eastward propagation is due to a lack of zonal asymmetry in the column-integrated MSE tendency anomalies relative to the MJO convective center in the simulation. Decomposition of the MSE tendency terms indicated that the biased MSE tendency distribution is primarily due to the vertical MSE advection term and surface turbulent fluxes. Further analysis showed that it is the unrealistic simulation of the MJO vertical velocity structure that results in the biased vertical MSE advection. In the observation, an upward (downward) motion anomaly is seen in upper troposphere to the west (east) side of the MJO convective center, but in the simulation the upward motion anomaly to the west is not seen, while the downward motion anomaly is weaker than observed. Such biased intraseasonal pressure velocity anomalies are probably due to the treatment of convective parameterization (Wang et al., 2017; Lin et al., 2004). Furthermore, the overestimated surface turbulent fluxes west of the MJO convection result from the notably overestimated Rossby wave response in the simulation, as the enhanced surface meridional wind anomalies associated with it lead to more evaporation over the northern and southern Indian Ocean.

It is worth mentioning that the overestimated Rossby wave circulation in the simulation mainly arises from the meridional wind anomalies, while the zonal wind component at the equator is similar (see Fig. 5(g, h)). We also calculated the Rossby wave intensity and Kelvin wave intensity based on the zonal wind anomaly as well as the R-K ratio defined by the Rossby wave intensity divided by the Kelvin wave intensity following Wang et al. (2018), as shown in Fig. S3. No significant difference could be found between the simulation and the observation.

The causes of the biased MJO propagation in HiRAM-C180 identified in the current study are different from previous studies based on multi-model simulations, which suggested that unrealistic simulation of horizontal MSE advection is critical in causing biased MJO propagation (e.g., Gonzalez and Jiang, 2017). This implies that it is necessary to conduct a detailed analysis of a given model to understand the specific reason for the model bias.

## Funding

This work was supported by the National Key Research and Development Program on Monitoring, Early Warning and Prevention of Major Natural Disaster [Grant No. 2019YFC1510004], the National Natural Science Foundation of China [Grant Nos. 41975108 and 42105022], NOAA [Grant No. NA18OAR4310298], the Natural Science Foundation of Jiangsu [Grant No. BK20190781], and the National Natural Science Foundation of China–Shandong Joint Fund for Marine Science Research Centers [Grant No. U1606405].

## Supplementary materials

Supplementary material associated with this article can be found, in the online version, at doi:10.1016/j.aosl.2022.100194.

## References

Ahn, M., Kim, D., Kang, D., Lee, J., Sperber, K.R., Gleckler, P.J., Jiang, X., et al., 2020. MJO propagation across the Maritime Continent: are CMIP6 models better than CMIP5 models? Geophys. Res. Lett. 47 (11), e2020GL087250. doi:10.1029/2020GL087250.

Chen, G., Ling, J., Zhang, Y., Wang, X., Li, C., 2022. MJO propagation over the Indian Ocean and western pacific in CMIP5 models: roles of background states. J. Clim. 35, 955–973. doi:10.1175/JCLI-d-21-0255.1.

Dee, D., Uppala, S., Simmons, A., Berrisford, P., Poli, P., Kobayashi, S., Andrae, U., et al., 2011. The ERA-interim reanalysis: configuration and performance of the data assimilation system. Q. J. R. Meteorol. Soc. 137, 553–597. doi:10.1002/qj.828.

Duchon, C.E., 1979. Lanczos filtering in one and two dimensions. J. Appl. Meteorol. Climatol. 18, 1016–1022. doi:10.1175/1520-0450(1979)0182.0.CO;2.

Gonzalez, A.O., Jiang, X., 2017. Winter mean lower tropospheric moisture over the Maritime Continent as a climate model diagnostic metric for the propagation of the Madden-Julian oscillation. Geophys. Res. Lett. 44, 2588–2596. doi:10.1002/2016GL072430.

Huffman, G.J., Adler, R.F., Morrissey, M.M., Bolvin, D.T., Curtis, S., Joyce, R., McGavock, B., Susskind, J., 2001. Global precipitation at one-degree daily resolution from multisatellite observations. J. Hydrometeorol. 2, 36–50. doi:10.1175/1525-7541(2001)002<0036:GPAODD>2.0.CO;2.

Jiang, X., Waliser, D.E., Xavier, P.K., Petch, J., Klingaman, N.P., Woolnough, S.J., Guan, B., et al., 2015. Vertical structure and physical processes of the Madden-Julian oscillation:

exploring key model physics in climate simulations. J. Geophys. Res. Atmos. 120 (10), 4718–4748. doi:10.1002/2014JD022375.
Kessler, W.S., Kleeman, R., 2000. Rectification of the Madden–Julian oscillation into the ENSO cycle. J. Clim. 13, 3560–3575. doi:10.1175/1520-0442(2000)0132.0.CO;2.
Kim, D., Kug, J.S., Sobel, A.H., 2014. Propagating versus nonpropagating Madden–Julian oscillation events. J. Clim. 27, 111–125. doi:10.1175/JCLI-d-13-00084.1.
Kim, D., Maloney, E.D., 2017. "Simulation of the Madden-Julian oscillation using general circulation models." Chap. 9 in The Global Monsoon System. Singapore: World Scientific. pp. 119–130, doi:10.1142/9789813200913_0009.
Li, T., 2014. Recent advance in understanding the dynamics of the Madden-Julian oscillation. J. Meteorol. Res. 28, 1–33. doi:10.1007/s13351-014-3087-6.
Li, T., Wang, B., 1994. The influence of sea surface temperature on the tropical intraseasonal oscillation: a numerical study. Mon. Weather Rev. 122, 2349–2362. doi:10.1175/1520-0493(1994)122<2349:TIOSST>2.0.CO;2.
Li, T., Ling, J., Hsu, P.C., 2020. Madden-Julian oscillation: its discovery, dynamics, and impact on East Asia. J. Meteorol. Res. 34, 20–42. doi:10.1007/s13351-020-9153-3.
Liebmann, B., Smith, C.A., 1996. Description of a complete (interpolated) outgoing longwave radiation dataset. Bull. Am. Meteorol. Soc. 77, 1275–1277. doi:10.1175/1520-0477(1996)077<1255:EA>2.0.CO;2.
Lin, J., Mapes, B., Zhang, M., Newman, M., 2004. Stratiform precipitation, vertical heating profiles, and the Madden–Julian oscillation. J. Atmos. Sci. 61, 296–309. doi:10.1175/1520-0469(2004)0612.0.CO;2.
Murakami, H., Vecchi, G.A., Underwood, S., Delworth, T.L., Wittenberg, A.T., Anderson, W.G., Chen, J.H., et al., 2015. Simulation and prediction of category 4 and 5 hurricanes in the high-resolution GFDL HiFLOR coupled climate model. J. Clim. 28 (23), 9058–9079. doi:10.1175/JCLI-d-15-0216.1.
Sobel, A.H., Maloney, E.D., 2000. Effect of ENSO and the MJO on western north pacific tropical cyclones. Geophys. Res. Lett. 27, 1739–1742. doi:10.1029/1999 gl011043.
Wang, B., Chen, G., 2017. A general theoretical framework for understanding essential dynamics of Madden–Julian oscillation. Clim. Dyn. 49, 2309–2328. doi:10.1007/s00382-016-3448-1.
Wang, B., Lee, S.-S., Waliser, D.E., Zhang, C., Sobel, A., Maloney, E., Li, T., et al., 2018. Dynamics-oriented diagnostics for the Madden-Julian oscillation. J. Clim. 31, 3117–3135. doi:10.1175/JCLI-D-17-0332.1.
Wang, L., Li, T., Maloney, E., Wang, B., 2017. Fundamental causes of propagating and nonpropagating MJOs in MJOTF/GASS models. J. Clim. 30, 3743–3769. doi:10.1175/JCLI-D-16-0765.1.
Wang, L., Li, T., 2020a. Effect of vertical moist static energy advection on MJO eastward propagation: sensitivity to analysis domain. Clim. Dyn. 54, 2029–2039. doi:10.1007/s00382-019-05101-8.
Wang, L., Li, T., 2020b. Reexamining the MJO moisture mode theories with normalized phase evolutions. J. Clim. 33, 8523–8536. doi:10.1175/JCLI-D-20-0202.1.
Wheeler, M.C., Hendon, H.H., 2004. An all-season real-time multivariate MJO index: development of an index for monitoring and prediction. Mon. Weather Rev. 132, 1917–1932. doi:10.1175/1520-0493(2004)132<1917:AARMMI>2.0.CO;2.
Xiang, B., Zhao, M., Jiang, X., Lin, S.J., Li, T., Fu, X., Vecchi, G., 2015. The 3–4-week MJO prediction skill in a GFDL coupled model. J. Clim. 28, 5351–5364. doi:10.1175/JCLI-D-15-0102.1.
Zhang, C., 2005. Madden-Julian oscillation. Rev. Geophys. 43, RG2003. doi:10.1029/2004RG000158.
Zhang, C., Ling, J., 2012. Potential vorticity of the Madden–Julian oscillation. J. Atmos. Sci. 69, 65–78. doi:10.1175/JAS-d-11-081.1.
Zhao, C., Li, T., 2019. Basin dependence of the MJO modulating tropical cyclone genesis. Clim. Dyn. 52, 6081–6096. doi:10.1007/s00382-018-4502-y.
Zhao, M., Held, I.M., Lin, S.J., Vecchi, G.A., 2009. Simulations of global hurricane climatology, interannual variability, and response to global warming using a 50-km resolution GCM. J. Clim. 22, 6653–6678. doi:10.1175/2009JCLI3049.1.
Zhou, W., Chan, J.C.L., 2005. Intraseasonal oscillations and the South China Sea summer monsoon onset. Int. J. Climatol. 25, 1585–1609. doi:10.1002/joc.1209.
Zhu, Z., Li, T., 2017. The statistical extended-range (10–30-day) forecast of summer rainfall anomalies over the entire China. Clim. Dyn. 48, 209–224. doi:10.1007/s00382-016-3070-2.